In situ monitoring of dislocation proliferation during plastic deformation using ultrasound

5 authors, including:

Vicente Salinas
University of Chile
13 PUBLICATIONS   **18** CITATIONS

SEE PROFILE

C. Aguilar
Universidad Técnica Federico Santa María
75 PUBLICATIONS   **331** CITATIONS

SEE PROFILE

Rodrigo A. Espinoza
University of Chile
35 PUBLICATIONS   **211** CITATIONS

SEE PROFILE

Fernando Lund
115 PUBLICATIONS   **1,747** CITATIONS

SEE PROFILE

Some of the authors of this publication are also working on these related projects:

"Nanostructured II-VI semiconductor materials and arrays: synthesis, characterization and field emission studies" View project

In-situ measurement of microstructural changes in Aluminum under traction test : Linear and nonlinear analysis View project

In situ monitoring of dislocation proliferation during plastic deformation using ultrasound

Vicente Salinas [a], Claudio Aguilar [b], Rodrigo Espinoza-González [c], Fernando Lund [a], Nicolás Mujica [a, *]

[a] Departamento de Física, Facultad de Ciencias Físicas y Matemáticas, Universidad de Chile, Avenida Blanco Encalada 2008, Santiago, Chile
[b] Departamento de Ingeniería Metalúrgica y Materiales, Universidad Técnica Federico Santa Maria, Av. España 1680, Valparaso, Chile
[c] Departamento de Ciencia de los Materiales, Facultad de Ciencias Físicas y Matemáticas, Universidad de Chile, Avenida Beauchef 851, Santiago, Chile

ARTICLE INFO

ABSTRACT

Ultrasound has long been used as a non-destructive tool to test for the brittle fracture of materials. Could it be used as a similar tool to test for ductile failure? As a first step towards answering this question, we report results of local measurements of the speed of transverse waves in aluminum under standard testing conditions at two different probe locations and continuously as a function of applied load. The result, as expected, is independent of stress in the elastic regime, but there is a clear change, consistent with a proliferation of dislocations, as soon as the yield strength is reached. We use a model that blames the change in wave speed on the interaction of elastic waves with oscillating dislocation segments, which quantitatively relates the change in wave velocity with dislocation density Λ and segment length L, thus obtaining a continuous relation between dislocation density and externally applied stress. We took off samples from the probe before, at intermediate, and high loading, and we measured their dislocation density using standard X-ray diffraction and transmission electron microscopy techniques. The results agree well with the acoustic measurements, and the relation between stress and dislocation density is consistent with the Taylor rule. This indicates that monitoring the speed of transverse waves could become a useful diagnostic of dislocation density for metallic pieces in service as well as a tool to test models of plastic behavior.

© 2017 Elsevier Ltd. All rights reserved.

1. Introduction

Dislocation density is a key variable to describe and possibly to control, the plastic behavior of metallic materials. In this paper we show that it is possible to measure, in situ, the dislocation density in aluminum as a function of applied stress, continuously, in a standard tension test using ultrasound.

In situ measurement of plastic behavior and thus, directly or indirectly, of dislocation density, has been a particularly active area of research in recent years, especially at the micro and nano scale, using transmission electron microscopy (TEM),

scanning electron microscopy (SEM) and atomic force microscopy (AFM). For example, in-situ TEM has been used by Oh et al. (2009) to perform tensile tests of submicrometer-sized single crystals of aluminum; this allowed them to directly observe dislocation nucleation and motion. Landau et al. (2010) similarly tested single crystal aluminum to study the evolution of dislocation patterns. Zhang et al. (2014) compressed steel nanoblades and were able to determine the relation between the evolution of the dislocation structures and the flow stress during deformation.

In situ mechanical testing that incorporated SEM with digital image correlation (DIC) was recently used by Guery et al. (2016) to measure displacement and strain fields in austenitic stainless steel. They were able to compare their results with crystal plasticity finite element simulations. A summary of a variety of in situ testings inside a SEM has been given recently by Rudolf et al. (2016). The use of AFM for in situ testing is much more recent. For example, Kahloun et al. performed slip measurements along the individual steps of plastically strained single crystal copper (Kahloun et al., 2016) and iron (Kahloun et al., 2013) in an AFM.

Dislocation density has long been the object of much modeling and analysis, with dislocation dynamics (DD) providing a powerful tool. This technique, in use for quite some time, considers dislocations in a continuum and discretizes them into segments whose motion is followed under the action of both external and self forces. Examples include the work of Bulatov et al. (2006), who predicted the existence of unusual elements of dislocation network topology and subsequently verified their existence both with atomistic simulations and TEM experiments in single-crystal molybdenum. Sills et al. (2016) have used DD with an efficient time integration scheme to compute the dislocation density as a function of strain in a work-hardening simulation of copper at 300 K up to 1.5% strain. Evolution equations have been proposed by Monavari et al. (2016) within a continuum approach, and a meso-scale scheme to treat the evolution of dislocation density functions has been developed by Leung and Ngan (2016) through a coarse graining procedure applied to large numbers of individual dislocations. Additional inroads into the vast literature are provided by the recent publications of Arsenlis et al. (2004), Lee et al. (2010) and Leung et al. (2015).

While in situ measurements using microscopy have been quite fruitful, particularly in relation to crystal plasticity, the fact remains that small samples, often with special preparation, are needed. At the macroscale, most measurements still rely on post-mortem studies, especially using X-ray diffraction (XRD) and TEM. These are intrusive tools, and not well suited to probe materials in service. In the long run, a non-intrusive tool would be highly desirable, and Ultrasound (US) appears as a natural candidate. Such technology is routinely used in the detection of cracks and flaws, and has been employed for decades as a non-destructive testing tool (McSkimin, 1961; Chen, 2007). Given the low energies involved, it can penetrate deep into a material without affecting it, and the detection of cracks and flaws in solid materials in service is a major field of application. The question naturally arises wether ultrasound can be used as a non-destructive testing tool for the plastic behavior of materials, including ductile failure, in the same way that it is used to test for brittle fracture. More precisely, the interaction of ultrasound with cracks and flaws provide an early warning that brittle fracture may occur. We wish, in the long run, to similarly use ultrasound as an early warning tool that ductile failure may occur. In order to achieve this aim, we take the first step in this paper and characterize the early stage of plastic behavior through the interaction of ultrasound with dislocations.

For a long time it has been known that ultrasound or, more generally, elastic waves, interact with dislocations ((Maurel et al., 2004), and references therein). Granato and Lücke (GL), in their classic work (Granato and Lücke, 1956a, 1956b), developed a theory of velocity decrement and elastic modulus change based on a treatment of dislocations as elastic strings in interaction with elastic waves. This GL approach has been widely used to interpret acoustic and ultrasonic measurements in metallic materials. Quite recently (Sobie et al., 2017), it has been used within a DD study of the bypassing of a self-interstitial atom loop by a dislocation. As discussed in some detail elsewhere (Maurel et al., 2005; Barra et al., 2015) however, GL theory has limitations, and two stand out: The first is an inability to discriminate between sound and transverse waves on the one hand, and screw and edge dislocations on the other. The second is accounting for the amplitude decrease of an elastic wave in terms of the internal losses at the dislocation location only, without consideration of the loss of coherence due to the multiple scattering. Both shortcomings were addressed in a generalized theory proposed by Maurel et al. (2005) and Rodríguez et al. (2009). Being able to distinguish between the interaction of longitudinal and transverse waves with dislocations provided an explanation not only to the fact that the ratio between the damping of longitudinal and transverse waves for polycrystalline copper (Ledbetter et al., 2011), copper single crystals (Ogi et al., 1999) and LiNbO$_3$ (Ogi et al., 2004) is independent of the microscopic details of the material, but it also provided a precise numerical value for that ratio, in agreement with the experimental data (Maurel et al., 2005). Including the effect of the loss of coherence in the amplitude attenuation of an acoustic wave, in addition to the effect of the internal losses suffered through the interaction with each individual dislocation, provided an explanation to the frequency dependence for ultrasound attenuation observed in copper by Zhang et al. (2004).

More recently, Mujica et al. (2012) used Resonant Ultrasound Spectroscopy (RUS) (Migliori et al., 1993; Leisure and Willis, 1997; Ogi et al., 2002), to measure the shifts in the speed of transverse waves within aluminum samples subject to various heat and mechanical treatments. They showed, using the generalized GL theory of Maurel et al., that variations in dislocation densities in aluminum at the 10^9 mm^{-2} level produced a shift in the speed of propagation of transverse waves at the 1% level, which can be measured with 0.15% accuracy. They also measured the dislocation density in the various samples using XRD, and showed results in agreement with those of RUS, with the latter providing not only a non-intrusive probe, but also better accuracy. These results were obtained with samples especially prepared for laboratory testing. The question now is: Can this technique be scaled to pieces in service?

One intermediate step that must be taken along this road is to see wether the dislocations that are generated by metals and alloys under standard testing conditions generate a shift in wave speed propagation that can be measured with available

hardware. This paper presents results of an experiment with aluminum that answers this question in the affirmative. In a previous work under similar conditions, Hirao et al. (2000) used the method of electromagnetic acoustic resonance (EMAR) to make a contactless average measurement of ultrasonic attenuation and velocity during fatigue tests of polycrystalline copper. They applied a sinusoidal load with an amplitude on the order of 100 MPa at a frequency of 10 Hz, and found that the specimens fractured after 10^4-10^5 cycles. Their measurements revealed that at between 20% and 40% of the total lifetime the acoustic attenuation shows a large peak, consistent with dislocation multiplication, rearrangement and subsequent mobility decrease. Min and Kato (2004) and Min et al. (2005) monitored the ultrasonic parameters of an aluminum alloy inside a water bag under cyclic loading (Min and Kato, 2004) and during tensile testing (Min et al., 2005). Water was used as an intermediate medium in order to minimize the losses that are produced at the sample-transducer interface. In the fatigue test (Min and Kato, 2004), samples were loaded at a frequency of 0.001 Hz and a stress amplitude of 50−150 MPa. The object of study was the material behavior as a function of time during one cycle, and, during this time interval, an oscillatory behavior of the propagation time of ultrasonic waves was observed. This result was interpreted in terms of the depinning and subsequent re-pinning of dislocations from point defects. In the tension test (Min et al., 2005), sound velocity and sample thickness were monitored in real time, and the results interpreted qualitatively in terms of dislocation multiplication and dislocation loop length variation.

In this work we describe quantitative measurements of the speed of transverse waves in aluminum as a function of stress in real time, for which the corresponding value for the density of dislocations is inferred. More precisely, the changes in the speed of transverse waves are directly related to the changes of the dimensionless quantity ΛL^2, where Λ is the dislocation density in units of length per volume, and L is the average length of the dislocation segments. In order to obtain, say, Λ by itself, the value of L must be otherwise retrieved. For example, from accepted values in the literature or from direct measurements, say using TEM. However, as discussed in the text below, the qualitative behavior of Λ is independent of the precise numerical value of L. Our results are compared with post-mortem studies using XRD and TEM. Section 2 describes the acoustic, XRD and TEM experimental procedures. Section 3 presents and compares the results concerning dislocation density obtained through the three techniques. Sections 4 and 5 present a discussion and conclusions respectively.

2. Experimental setup and procedures

2.1. Velocity measurement

Fig. 1 presents details of the probes and a schematic drawing of the experimental setup. The probes were fabricated out of commercially 1100 pure aluminum (99.0% pure) with a geometry that is defined in the standard ASTM-E8/E8M for tensile tests (ASTM, 2013). Here, we present results obtained with a sample cut by Electrical Discharge Machining (EDM). Consequently, the parallelism of opposite faces is better than $0.3°$, which results in variations of width that are smaller than 60 μm over a distance of 12.5 mm. Details are given in Fig. 1 (a).
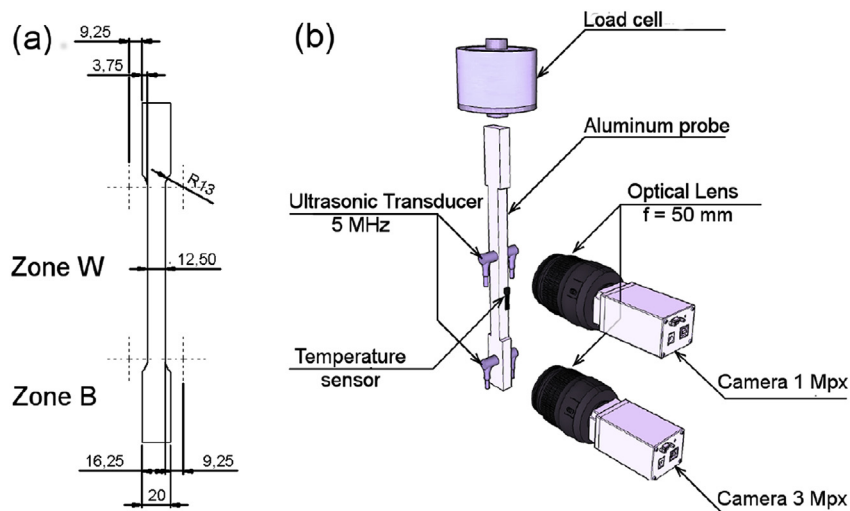

Fig. 1. (a) Aluminum probe dimensions under standard ASTM E8/E8M. Samples are 240 mm long and have a rectangular cross section, with symmetric top and bottom parts, 50 mm long, that have a larger cross area (10×20 mm^2). The central part, about 120 mm long, has a smaller cross area (10×12.5 mm^2). The central part and the symmetric top and bottom sections are separated by transition zones 9.13 mm long. (b) Schematic of the experimental setup. Two pairs of ultrasonic transducers are fixed to the sample, one at zone B and the other at zone W. Each pair of transducers is held with a constant compression force using a holder and a system of springs (not shown in the figure for simplicity). The local width at each zone is measured by images acquired with digital cameras.

Tensile tests are performed with an Instron 3369 machine. The maximum load capacity is 50 kN, which implies a maximum stress of 250 MPa in the large cross section areas and of 400 MPa in the smaller cross section central part. These values are well suited in the range of aluminum yield stress and ultimate stress. Special grips from Instron are used due to the ductile nature of aluminum in order to minimize sliding. The tensile tests are performed at an initial speed of 0.01 mm/min for loads lower than 3.5 kN (elastic regime) and later at 0.03 mm/min for larger loads (plastic regime). The tests are then considered as quasi-static, but at the same time have a maximum duration of 10 h, which cannot be much longer for operation conditions. For some tests, the probes were compressed back, at a speed of 0.03 mm/min, until the applied load was null.

In Fig. 1(b) we present a schematic representation of the experimental setup, including the most important elements. Two pairs of transverse wave ultrasonic transducers (Olympus V157-RM) are placed in contact with the probe using an ultrasonic couplant. One pair is placed at the base (zone B) and the other at the center of the probe (zone W), each corresponding to the large and small cross sectional area, respectively. The ultrasonic transducers are centered at 5.49 MHz and have a wide frequency response (of 5.5 MHz for −6 dB). Additionally, two strain gages (Omega KFH-3-350-C1-11L1M2R) are placed in the vicinity of each pair of ultrasonic transducers in order to measure the local strain. The strain gages are 3 mm long and their maximum deformation is 3%. Their voltage signals are measured with a Wheatstone bridge in configuration quarter-bridge and acquired by a analog to digital converter (National Instruments NI PCI-6381), which insures a voltage resolution of 3.8 μV, thus a precision of 0.635 μm/m. Finally, an integrated-circuit temperature sensor (Texas Instruments LM35) is placed between the two ultrasonic transducer pairs allowing precise temperature measurements (0.01 °C).

The wave speeds are determined by measuring the time of flight of short ultrasonic pulses. These consist of carrier signals with frequency 5 MHz modulated by a Gaussian curve, resulting in short pulses of 5 cycles. The carrier's wavelength is $\lambda = 0.62$ mm and the total pulse length is ≈ 3.1 mm, which indeed is short compared to the pulse propagation distance (10 mm). The excitation signal is generated by a Labview program that is sent to a waveform generator (Agilent 33500B) by means of a General Purpose Interface Board (NI GPIB-USB-HS). This excitation signal is then amplified by a high-power bipolar amplifier (NF Techno Commerce BA4850). Both the excitation voltage signal and the measured received signal are acquired by a high speed oscilloscope (Lecroy Wavejet 334A). All the ultrasonic signals are then transferred to a personal computer (PC) with the same GPIB protocol. The time of flight is then obtained by computing the cross correlation between the excitation and received signal envelopes, which in turn are computed as the absolute values of their Hilbert transforms. The final time resolution is 1 ns.

During the tensile tests the probe's cross sectional area decreases. In particular, each transverse dimension decreases. In the elastic regime this is quantified by the Poisson ratio ν. Because the wave speed is determined as the ratio between the time of flight and the probe width, we need to quantify these variations. This is done locally at each zone B and W by means of two digital cameras, of resolutions 3 MP and 1 MP respectively. As variations in the lower strain region (zone B) are expected to be smaller, the camera with the better resolution is used. The final spatial resolutions are 5.7 μm/pixel and 8.5 μm/pixel for zones B and W respectively.

The tensile testing machine provides the measurement of the total load during the probe's deformation. Additionally, we measure synchronously all the other physical relevant quantities, such as the emitted and received signals, the local strains, the sample's temperature and the images of each camera that capture the local width at each transducer pair location. This is done by means of an analog trigger connector included in the tensile testing apparatus, which triggers the data and image acquisition from the PC, which runs an in-house developed Labview program.

Temperature variations were kept small during the experimental runs, with a maximum variation of about 3 °C. There are two important reasons to do so: First, the strain versus voltage measurements are temperature dependent, which is measured by a proper calibration. Thus, the real strain is computed by making this temperature correction. Second, the sample also varies its volume by thermal expansion. This cannot be detected by the image analysis. Simultaneous time of flight and temperature measurements with no load applied to the samples allow us to calibrate and correct this effect. For both corrections, the data are computed with the reference temperature $T = 25$ °C.

2.2. Post-mortem characterization

To quantify and compare dislocation density and length, we performed post-mortem analysis by XRD and TEM. Three samples were prepared: (1) a first sample from the original aluminum plate (*Ori*); (2) a second sample from zone B (*PB*); (3) a third sample from zone W (*PW*). The original material was obtained by a laminating process, so it has an initial dislocation density. Samples PB and PW are cut from the probe after a third plastic tensile test. We remind that for a given tensile test, and because of their different cross sections (see Fig. 1), samples PB and PW are under lower and larger stress, respectively. The expected sample order, from low to high dislocation density, should be: *Ori*, *PB* and *PW*.

2.2.1. XRD characterization

X-ray powder patterns of the samples were collected on a multi purpose powder diffractometer STOE STADI MP equipped with a DECTRIS MYTHEN 1K detector and using pure Cu $K\alpha_1$-radiation ($\lambda_{\mathrm{XRD}} = 1.54056$ Å, curved Germanium (111) mono-chromator of the Johann-type). The microstructural parameters (lattice parameter a, microstrain $\langle \varepsilon^2 \rangle^{1/2}$) were obtained from Rietveld refinements of the X-ray powder patterns (see appendix) using the software Materials Analysis Using Diffraction (MAUD) (Lutterotti and Scardi, 1990) and using LaB_6 ($a = 4.1565915(1)$ Å) as external standard also for determining instrumental broadening (Scardi et al., 1994). It has been shown that the dislocation density Λ is proportional to the mean

square strain $\langle \varepsilon^2 \rangle$ (Williamson and Smallman, 1956; Krivoglaz, 1969). Therefore, the dislocation density values can be estimated by the equation proposed by Adler and Otte (1966) and Adler et al. (1970), which will be discussed below. The advantage of this equation is its mathematical simplicity. The Rietveld method is perhaps the best microstructural refinement procedure for polycrystalline materials using X-ray diffraction data (Mittemeijer and Scardi, 2004). Its main advantages are: i) it uses directly the measured intensity points; ii) it uses the entire X-ray pattern; iii) it is less sensitive to model errors and iv) it is less sensitive to experimental errors (Will, 2006).

An alternative method to obtain the dislocation density in materials with cubic and hexagonal crystal structure by fitting the whole profile was developed by Ungár and collaborators (Ungár et al., 2001). We attempted this method but obtained high errors ($> 1000\%$) in the evaluated parameters. Moreover, the errors were very sensitive to the choice of initial parameters. Furthermore, this method limits the morphology of the crystallites to be either spherical or ellipsoidal. Instead, in the Rietveld method (using MAUD software), anisotropic functions for crystallite shape and microstrain can be used (Popa, 1998). Therefore, considering the advantages mentioned above and the possibility to use anisotropic functions, the Rietveld method was implemented to estimate dislocation density values, using Eqns. (2) and (3) defined below.

The X-ray pattern includes reflection broadening, which is a function of crystallite size (D) and mean square strain $\langle \varepsilon^2 \rangle$. The two effects can be separated on the basis of the different diffraction-order dependence of X-ray reflection broadening. Symmetrical broadening is caused by the presence of dislocations and intrinsic stacking faults in deformed metals, and asymmetrical broadening can arise from twin faults, extrinsic faults, solute segregation at stacking faults, and nonuniform distribution of residual stresses. The relationship between crystallites size (D), mean square strain $\langle \varepsilon^2 \rangle$ and reflection broadening $\Delta\theta$ when materials exhibit isotropic strain is given by

$$\Delta\theta \cos\theta = \left(\frac{\lambda_{\text{XRD}}}{D} \right) + \left(2\langle \varepsilon^2 \rangle \sin\theta \right), \tag{1}$$

where θ is the Bragg angle for the *hkl* reflection.

Popa (1998) proposed a relationship between the anisotropic broadening of the diffracted reflections produced by crystallite size and microstrain for different crystalline structures. The specific equations that provide the dependence of crystallite size and microstrain on Miller indices (*hkl*) for cubic symmetry can be found in (Popa, 1998). There are different methods to estimate the dislocation density from XRD patterns, but most of them are based in knowledge of the microstrain values. Williamson and Smallman (1956) proposed a simple expression to determine the dislocation density from strain broadening of XRD reflections, given by the set of equations

$$\Lambda = \frac{24\pi E}{GF} \frac{\langle \varepsilon^2 \rangle}{a^2}, \tag{2}$$

$$F = \frac{\ln\left(\frac{R_0}{r_0}\right) + 0.77 n_d}{\ln\left(\frac{R_0}{r_0}\right)}, \tag{3}$$

were E is the Young's modulus and G is the shear modulus. The E and G values for aluminum are 73.3 GPa and 27.4 GPa, respectively (Mujica et al., 2012). The model is based on dislocation array and a strain energy factor F, which allows for the effect of dislocation arrangement. In metals, the cold workhardening is produced by piling up of dislocations against barriers in the slip plane, which causes a large increase in the strain energy per dislocation. If there are n_d dislocations in each pile-up, they act to a first approximation as one dislocation of Burgers vector $n_d b$, and hence the strain energy is increased from $n_d \xi$, to $n_d^2 \xi$ (since it is the square of the Burgers vector that determines the energy of a dislocation ξ). Polygonization decreases the strain energy because dislocations can climb from slip planes to form bend planes, which cancels their long-range stress fields at distances greater than the separation of dislocations in the bend plane. Finally, the energy of each dislocation is reduced and F values can be determined with Eqn. (3). The strain energy factor F takes into account the fact that dislocation strain fields may interact, changing the strain energy, which is proportional to the mean square strain. This result can be obtained from the Seeger and Kronmüuller equation (Seeger and Kronmuller, 1962), were n_d is the number of dislocations per domain ($n_d = 25$ for FCC crystals). R_0 is outer cut-off radius, which in general takes values between 40 and 50 times b, with b the Burgers vector. r_0 is the effective core radius, which is between $b/2$ and b. Consequently, we estimate that in our system $F \approx 5$ (more details are given in Seeger and Kronmuller (1962)).

2.2.2. TEM characterization

Samples for TEM measurements were prepared following a procedure that minimizes possible modifications of the aluminum microstructure. Slices of about 500 μm thickness were cut from original aluminum and from deformed samples in transversal direction. Then, disks of 3 mm diameter were cut by electroerosion and gently polished until reaching a thickness of 100 μm. The final perforation was performed by electro polishing using an electrolyte of 90 mL of distilled water, 730 mL of ethanol, 100 mL of 2-butoxyethanol and 78 mL of percloric acid, in a double jet Tenupol 5 (Struers) with a voltage of 40 V at

5 °C. A FEI microscope model Tecnai F20 G^2 STwin was used for TEM observations, operated at 200 kV. Measurements of dislocation density by TEM were performed by tilting the samples to orient grains to a zone axis [111] with the aim of visualizing (111) planes because in fcc metals, the main slip system for dislocations is (111)[110]. Then, the Weak Beam Dark Field (WBDF) technique (Williams and Carter, 2009) was employed to enhance the dislocation contrast.

3. Results

3.1. In situ ultrasound - elastic regime

Before plastic deformations are performed, we carry out three elastic deformations. We do this to verify that the elastic wave speed does not change, or changes very little, for deformations within the elastic regime. Additionally, this allows the strain gauges and machine grips to "settle" onto the probe. An example of the third elastic tensile and consecutive compression tests are shown in Fig. 2(a) with data obtained from zone B. At the deformation speeds we have used, these are reversible curves. For zone W the results are qualitatively very similar, except that the local stress increases up to ∼ 30 MPa.

The measured transverse elastic wave speeds vary less than 2 m/s during the complete elastic test (For an example see Fig. 2(b)). During the three consecutive elastic tests it either varies randomly around a mean value or it shows a slow systematic trend to either increase or decrease (but always less than 2 m/s). For zone B, the measured wave speeds during the three consecutive tensile deformations, from 0 MPa to 19 MPa, are $v_T = 3104.7 \pm 0.3$ m/s (test 1), $v_T = 3105.7 \pm 0.2$ m/s (test 2) and $v_T = 3106.2 \pm 0.2$ m/s (test 3). For zone W, the measured wave speeds while varying the stress from 0 MPa to 30 MPa, are $v_T = 3116.2 \pm 1.9$ m/s (test 1), $v_T = 3118.8 \pm 0.8$ m/s (test 2) and $v_T = 3119.3 \pm 0.8$ m/s (test 3). To a first approximation, these values are all constant. However, small variations may be due to slight re-accommodation of the ultrasonic transducers, which may become more or less well aligned during the tensile and compression tests because during the deformation a small rotation of the probe around its principal axis certainly occurs. The differences of order 10 m/s between zone B and W can be attributed to the differences in spatial resolution of the two cameras. We have performed many load-free measurements with differing locations of the transducer pairs to estimate the error due to alignment variation, which we calculate is on the order of $1 - 2$ m/s. Therefore, changes of this order of magnitude are attributed to changes of transducer accommodations on the probes.

3.2. In situ ultrasound - plastic regime

We now turn to the results obtained within the plastic regime. In Fig. 3(a) we show the stress versus strain curves obtained from zone W for three consecutive tensile tests, each one finishing at a larger maximum stress. The yield stress σ_Y increases with the number of tests, which is the well-known workhardening process induced by the proliferation of dislocations ((Abbaschian and Reed-Hill, 2008), Chap. 5). The corresponding yield stresses, computed by the method proposed by Christensen (2008), are 29.8 ± 0.4 MPa, 43.8 ± 0.3 MPa, 51.1 ± 0.5 MPa, respectively. We emphasize that this method uses the data from the stress versus strain curve, specifically by imposing $(d^3\sigma/d\varepsilon^3)|_{\varepsilon_Y} = 0$ and then computing $\sigma_Y = \sigma(\varepsilon_Y)$. This definition considers the point $(\varepsilon_Y, \sigma_Y)$ for which the tangent modulus is changing at the fastest rate for increasing strain. In Fig. 3(b) we present the corresponding transverse elastic wave speeds measured during these same deformation tests. Here, the data is presented in semi-log scale to emphasize the abrupt changes that occur for $\sigma > \sigma_Y$. For each new test, the initial wave speed is very close to the final wave speed at the end of the previous test. Additionally, for $\sigma > \sigma_Y$, the measured velocity data appear to collapse onto a single curve regardless of the initial condition.
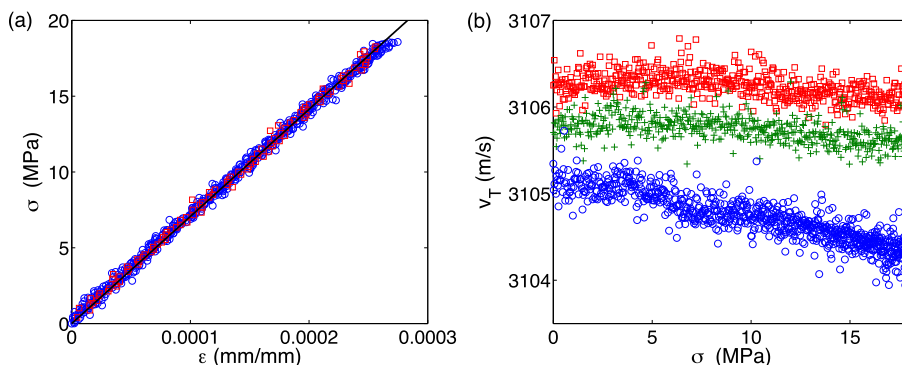

Fig. 2. (a) Third elastic tensile (∘) and compression (□) tests on sample in zone B. The data is fitted to $\sigma = E\varepsilon$ (continuous line), where E is the Young's modulus. We obtain $E = 70.7 \pm 0.2$ GPa for zone B and $E = 72.2 \pm 0.2$ GPa for zone W. The R^2 regression coefficients are 0.996 and 0.997 respectively. (b) Transverse wave speed v_T versus stress σ during the first (∘), second (+) and third (□) elastic tensile tests (zone B).
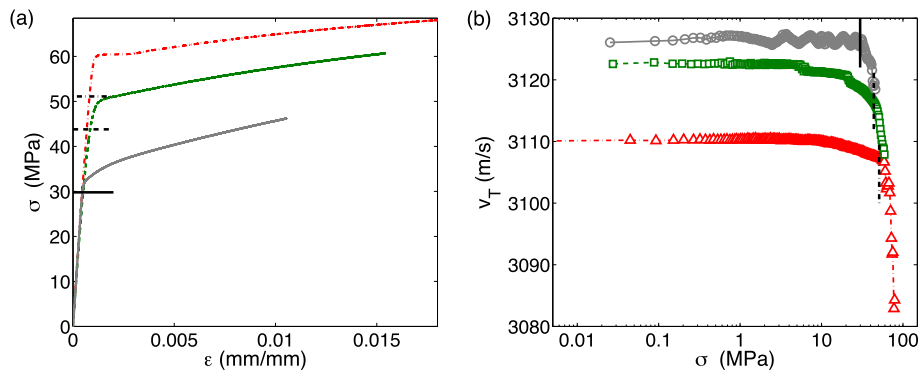
Fig. 3. (a) Stress-strain curves for three consecutive tensile tests (zone W). The yield stress increases for each consecutive test. (b) v_T versus σ in semi-log scale for the same tensile tests (first: $\circ$, second: $\square$ and third test: $\triangle$). Each new test starts with a wave speed that is very close to the final value of the previous test. The wave speed decreases abruptly at $\sigma \sim \sigma_Y$ and all curves colapse in the plastic regime. The horizontal and vertical lines, in (a) and (b) respectively, correspond to the measured yield stress following Christensen (Christensen, 2008).

3.3. XRD results

Fig. 4 shows the Rietveld refinement with low figures of merit. The high quality of the refinement can be checked by the *R*-values (see equations (17) and (18) in the appendix). Four peaks in the full profile are observed, which correspond to different crystallographic diffractions, specifically corresponding to diffractions with *hkl* indices: (200) ($2\theta = 44.70°$), (220) ($2\theta = 65.05°$), (311) ($2\theta = 78.17°$) and (400) ($2\theta = 99.03°$). The first diffraction peak exhibits three main crystallite size distributions (phases) of Al (inset of Fig. 4). Here, three phases of aluminum can be identified (Al_1: yellow, Al_2: purple and Al_3: green lines in the inset of Fig. 4), and each one corresponds to different aluminum crystallite sizes produced by the deformation of a unitary cell with a slightly different lattice parameter.

To account for the microstructure of the phases, we performed profile fittings by considering Popa line broadening (Popa, 1998) and an anisotropic strain-size model using Popa Rules. In addition, given we observed texture in all XRD patterns, we implemented an arbitrary texture model. For samples Ori and PW, two main crystallite size distributions of Al were determined; whereas sample PB exhibits three. The value of microstrain and average crystallite size for each sample and phase are shown in Table 1.

To quantify the contribution to the global dislocation density from different microstructural phases of aluminum (Al_m), we proceed as follows: First, using the microstrain $\langle \varepsilon^2 \rangle^{1/2}$ of each phase we use Eqn. (1) to get the corresponding crystallite size *D*. Then, using Eqns. (2) and (3) we obtain Λ_j for each phase. By integrating the complete diffraction profile (I_{cp}) and then the diffraction profile (I_{ph}^j) of each phase found by the Rietveld method, we obtain the fraction I_{ph}^j / I_{cp} of each phase that contributes to the global surface dislocation density. Thus, the average dislocation density is

$$\Lambda = \sum_{j=1}^{N_{ph}} \frac{I_{ph}^j}{I_{cp}} \Lambda_j, \tag{4}$$

where N_{ph} is the number of phases that contribute to the XRD profile.

Finally, we note that despite the low errors that are obtained for $\langle \varepsilon^2 \rangle$ and *D*, relatively larger errors for Λ are reported in Table 2, which vary between $\approx 35\%$ and 50%. These come from the contribution of the different Al phases in the computation of the average dislocation density (Eqn. (4)).

3.4. TEM results

Fig. 5 presents a typical TEM image obtained from sample Ori, which shows that dislocations are clearly visible. The total length, L_t, of all dislocations in each image was measured by ImageJ software, as well as the image area, *A*, from the calibrated scale of the microscope.

The dislocation density was obtained as the total length of dislocations divided by the volume in the area of interest, which required us to measure the thickness *e* of the TEM sample. This was done using Convergent Beam Electron Difraction (CBED) images at the [111] zone axis orientation. These were later compared with CBED images simulated at the same orientation by JEMS electron microscopy simulation software, of different thickness of aluminum samples. The average dislocation length and its associated error are then computed by the mean and standard deviation of measured dislocation lengths. Surface dislocation density was computed as $\Lambda = L_t/(eA)$. By this procedure, we obtained the values reported in Table 2. Here, we also include the surface dislocation density obtained by XRD, the number of analyzed images and the amount of dislocations measured for each sample.
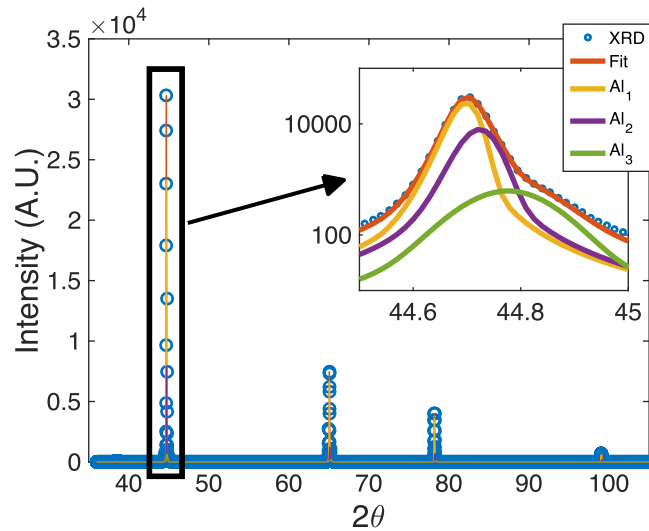
Fig. 4. Full XRD profile for sample PB, with $2\theta = [35°-105°]$. Four peaks are detected, corresponding to different crystallographic diffraction directions: (200) $(2\theta = 44.70°)$, (220) $(2\theta = 65.05°)$, (311) $(2\theta = 78.17°)$ and (400) $(2\theta = 99.03°)$. Inset: The first diffraction peak exhibits three main crystallite size distributions of Al, their contributions to the fit are shown in semi-log scale, Al_1 (yellow) Al_2 (purple) and Al_3 (green). (For interpretation of the references to colour in this figure legend, the reader is referred to the web version of this article.)

Table 1
Results from Rietveld method analysis of XRD data. The values of root mean square microstrain $\langle \varepsilon^2 \rangle^{1/2}$ and crystallite size D are presented with their respective errors. Different phases of aluminum are present in the diffraction profile.

	Phase	$\langle \varepsilon^2 \rangle^{1/2}$	error of $\langle \varepsilon^2 \rangle^{1/2}$	D (nm)	error of D (nm)
Ori	Al_1	5.3×10^{-4}	2.9×10^{-6}	1460	26
	Al_2	7.5×10^{-4}	1.01×10^{-5}	78	2
PB	Al_1	6.3×10^{-4}	5.2×10^{-6}	380	14
	Al_2	-4.6×10^{-4}	1.05×10^{-5}	228	15
	Al_3	-1.25×10^{-3}	6.3×10^{-5}	66	5
PW	Al_1	1.1×10^{-3}	3.4×10^{-6}	267	4
	Al_2	1.0×10^{-3}	5.3×10^{-5}	105	10

Table 2
Dislocation density obtained by XRD and TEM. For TEM, results were obtained using ImageJ. The average dislocation length and the number of images and dislocations that were analyzed are also provided.

	Ori	PB	PW
$\Lambda_{XRD} \times 10^7$ (mm^{-2})	8.12 ± 2.89	10.20 ± 5.48	26.50 ± 12.30
$\Lambda_{TEM} \times 10^7$ (mm^{-2})	1.1 ± 0.6	4.0 ± 2.0	13.0 ± 5.0
L (nm)	144 ± 65	65 ± 52	49 ± 31
No of images analyzed	5	6	8
No of dislocations detected	16	28	66

In Fig. 6 we present the set of all dislocation lengths L measured by TEM image analysis for each sample. Each measured L is shown, as well as the average and standard deviation per sample. We can conclude that for the three characterized samples, the dislocation length can be considered, at first approximation, as a constant, $L \approx 80$ nm.

3.5. Combining US, TEM and XRD

Using the analysis reported by Mujica et al. (28), we can relate the measured changes in wave speed reported in Fig. 3 to changes in the surface dislocation density Λ using

$$\frac{\Delta v_T}{v_T^0} = -\frac{8\Delta(\Lambda L^2)}{5\pi^4},$$
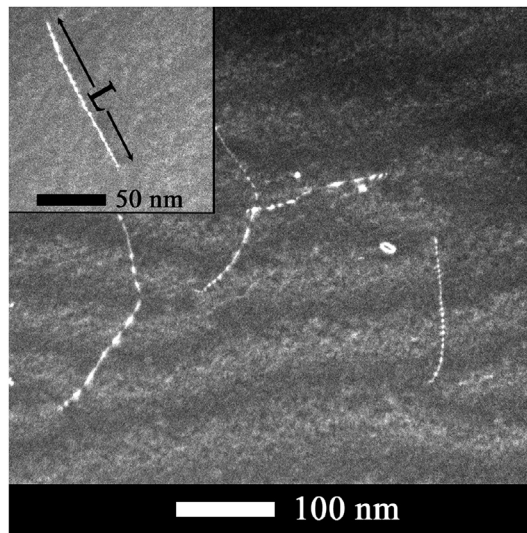
(5)

Fig. 5. TEM image from sample Ori obtained with the WBDF technique. Insert: TEM image from the same sample at 50 nm scale, from which it is possible to measure the length of each dislocation.

where L is the dislocation length. Here, we use $\Delta v_T = v_T - v_T^0$, where v_T is the measured wave speed and v_T^0 is the initial value, that is, before the first plastic deformation. The dislocation density variation is $\Delta\Lambda = \Lambda - \Lambda_0$, where Λ_0 is the initial dislocation density before the first plastic deformation. Using $L = 80$ nm and $\Lambda_0 = 4.6 \times 10^7$ mm^{-2} in Eqn. (5), the latter being the average of dislocation densities of sample Ori obtained by TEM and XRD characterizations, it is possible to plot the dislocation density during the different tensile tests on the specimen. Notice that this is a continuous monitoring of dislocation density as a function of stress, a measurement that would be impossible to perform either with XRD or TEM for pieces in service, given their intrusive nature. In Fig. 7 we present such analysis, namely the dislocation density obtained by ultrasound, continuously as a function of applied stress and for the three consecutive tensile tests. We also include results obtained by TEM and XRD characterizations performed on the original and post-mortem samples (PB and PW). The values obtained with XRD and TEM have significant error bars. Within the error bars, results obtained with XRD agree well with the values obtained through the acoustic measurements. The TEM results are, in general, lower than those obtained by XRD and ultrasound, although they show the same trend to increase as function of the applied stress.

4. Discussion

4.1. Dislocation density and dislocation length

As pointed out in the Introduction, our analysis of the acoustic measurements reported herein rely on the generalized Granato-Lücke theory developed by Maurel et al. (21). In this theory the dislocations are treated as pinned dislocation segments with (average) distance L between the pinning points. These dislocation segments are, in turn, treated as vibrating strings. As such they respond to a propagating elastic wave, influencing its behavior. This influence translates into the presence of an effective index of refraction for the wave propagation, giving an effective velocity v_T that is different from the velocity v_T^0 for the original sample before any plastic deformation test. For wavelengths much larger than L, a condition that is easily satisfied for the acoustic frequencies employed in our experiments, the change in propagation velocity is (Maurel et al., 2005; Mujica et al., 2012)

$$\frac{\Delta v_T}{v_T^0} = -\frac{8\Delta(nL^3)}{5\pi^4}, \tag{6}$$

with n the number of dislocation segments per unit volume. Assuming $nL = \Lambda$, Eqn. (5) follows. The dimensionless quantity $nL^3 = \Lambda L^2$ is therefore determined with as much accuracy as is available from the ultrasonic measurements. However, if the object of study is Λ, independent information about L must be provided. There are a number of ways of achieving this. One, which we have followed in the present paper, is to determine L through TEM measurements. While this is a very direct measurement, it is intrusive and cumbersome.

A tempting alternative to independently determine L is to measure, in addition to the change in acoustic velocity, acoustic attenuation as a function of frequency, which involves ΛL^4 (21). Up to now, we have used velocity measurements, rather than
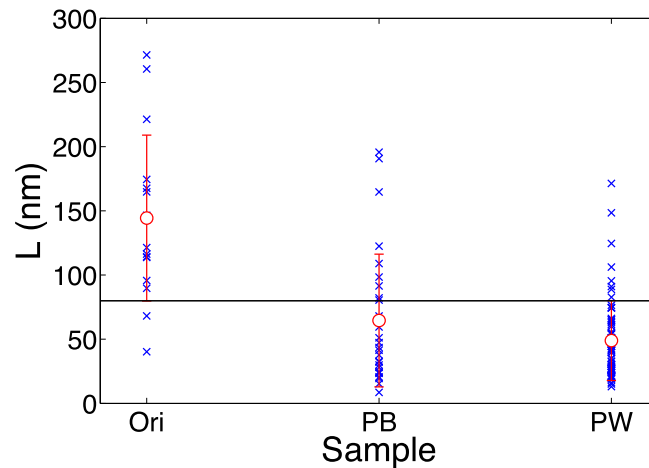
Fig. 6. Summary of dislocation length analysis obtained by TEM characterization. Each symbol (×) corresponds to a measured length. Open circles (∘) are the averages and error bars are computed by the standard deviation. The two horizontal lines (almost on top of each other) show the range of values that is common in all samples, namely from 79 to 80 nm.

acoustic attenuation measurements, mainly because for low and moderate dislocation content the corresponding effective absorption coefficient is very low, which makes precise measurements a more difficult task.

In any case, there is important qualitative information, such as the Taylor rule discussed below, that does not depend on the precise numerical value of L, but only on its order of magnitude. Note that, in this paper we consider the response of pinned dislocation segments to an elastic wave. This pinning can be provided by other dislocations, point defects, grain boundaries and, most importantly, by impurities (Hirth, 2012). Consequently, there need not be a specific relation between L and a characteristic wavelength of dislocation patterns as considered in similitude type arguments (Kuhlmann-Wilsdorf, 1985; Kubin et al., 2008; Devincre et al., 2008; Zaiser and Sandfeld, 2014).

4.2. Advantages and difficulties

In order to obtain our velocity precision, of the order of 0.1%, we need to measure very precisely both the ultrasonic pulse time of flight and the sample thickness. Our ultrasonic measurements are not only very precise and non-invasive, they can also be done continuously as function of the applied stress. We also stress that the equipment cost is much lower than the traditional TEM and XRD techniques that are commonly used for dislocation density characterization. Some difficulties that appear in our analysis are the high level of parallelism that our samples need as well as the appearance of some torsion in the sample that might affect transducer accommodation and its emission or reception direction. Additionally, samples cannot be too thin because the ultrasonic propagation length needs to be larger than transducer's far field distance, $L_{\text{ff}} = D_T^2/(4\lambda)$ (≈ 3.5 mm in our case), where D_T is the transducer diameter and λ the ultrasonic wavelength.

The velocity measurements provide a quantification of the density of dislocations with respect to a reference point. In our case this is the initial state of the sample. Since we use a single sample, the possible effect of impurities cancels out. Also, the wavelengths employed, on the order of 1 mm, are much larger than the size of crystallites so the effect of grain boundaries on the wave propagation is the same all along.

TEM measurements can provide values for both Λ and L through direct counting. Since this counting is done on a very small area of the sample, several measurements must be taken at different sites. The results we have obtained for L are presented in Fig. 6 and for Λ in Fig. 7. The value for the dislocation density Λ is, in general, lower than the value obtained through XRD, although it does show the same increasing trend as function of the applied stress. This behavior can be attributed to the large number of degrees of freedom present in the visualization of dislocations by TEM. The most significant parameter is the ability to spatially orient the sample in an optimal diffraction condition for the correct visualization of the dislocations, this reduces the visualized regions and thus the dislocation density obtained (see also (Wang et al., 2004)).

4.3. Extension to other materials

The proposed ultrasonic methodology is applicable to materials with high Peierls barriers. Indeed, the Peierls barrier for aluminum is of the order of 1 MPa (Kamimura et al., 2013). Using a laser Doppler interferometer we have measured an amplitude displacement of 2 nm at the ultrasonic transducer surface at 5 MHz (data not shown). This has been used as input in a finite element simulation of our Al sample, the result being that the average von Mises stress along the ultrasonic beam is 2.5 MPa (data not shown). For materials with larger Peierls barriers, higher intensity ultrasound will be needed to trigger the dislocation oscillation. Higher power transducers should then be used, with which the linear ultrasonic propagation can
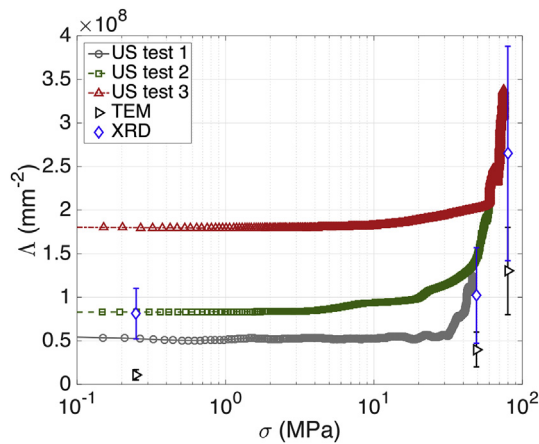
Fig. 7. Surface dislocation density Λ versus σ obtained from US data, presented in semi-log scale, for zone W and $L = 80$ nm. The data is from the same tensile tests shown in Fig. 3(a) (first: ∘, second: □ and third test: △). Additionally, the dislocation density obtained with TEM (▷) and XRD (⋄) are presented for samples Ori, PB and PW, with their corresponding error bars. For sample Ori we use an arbitrary value $\sigma = 0.25$ MPa, low enough to ensure that the corresponding measured Λ should be equal to the dislocation density obtained from US, because for the latter measurements are done well in the linear elastic regime. Samples PB and PW were cut from the probe after the third plastic tensile test; their stress values correspond to the maximum measured value at zones B and W ($\sigma_{max} \approx 49$ MPa and 80 MPa respectively).

always be analyzed. Indeed, for larger amplitudes, non-linear effects will start to be important, which in practice means that energy from the linear wave created by the source will be transferred to higher order modes (harmonics), but the linear propagation can always be measured.

The proposed methodology could also be extended to materials with one compact slip system, such as hcp, which will, in general, have a higher yield stress than aluminum. The ultrasound method we use is sensitive to the density of dislocations, and not to the actual mechanism of their creation. Consequently, once dislocations start to proliferate the acoustics should be able to pick up their presence. The hardware used in this work can measure the speed of shear waves with an accuracy of about 0.1%, which implies a similar accuracy for the quantity ΛL^2. Thus, the accuracy of Λ will be given by the precision with which the average L can be determined. The theory, as used here, relies on an average over all dislocation orientations, as well as slip plane orientations (Maurel et al., 2005). It should be possible to extend the theory to account for a different response of slip systems, and different Burgers vector, to the elastic waves, but this task is beyond the scope of the present work.

4.4. Workhardening and the Taylor rule

Finally, we turn to the workhardening that our sample undergoes during the consecutive tensile tests. As briefly discussed before, see Fig. 3(a), the sample's yield stress increases after each plastic deformation because of the proliferation of dislocations. Indeed, the Taylor rule relates flow stress τ and the density of dislocations Λ through

$$\tau = \tau_0 + \alpha b G \sqrt{\Lambda}, \tag{7}$$

where α is a dimensionless constant that indicates the interaction strength between dislocations (Gubicza et al., 2007), and τ_0 is the shear friction (*i.e.* the shear required to move an isolated dislocation, related to the Peierls resistance (Viguier, 2003)). Additionally, it has been shown that the measured mechanical stress σ and dislocation density Λ obey

$$\sigma = \sigma_0 + \alpha M b G \sqrt{\Lambda}, \tag{8}$$

where σ_0 is the friction stress and M is the reciprocal Schmid factor, which relates stress and shear through $\sigma = M\tau$.

Using Eqn. (8) we have fitted the measured stress σ as function of Λ using the appropriate values for aluminum ($G = 27.4$ GPa (Mujica et al., 2012), $b = 0.2863$ nm and $M = 3$ for untextured polycrystalline materials). The fitting procedure was done with the restriction $\sigma > \sigma_Y$ for each tensile test. The adjusted parameters are $\alpha = 0.1732 \pm 0.0003$ and $\sigma_0 = 1.57 \pm 0.11$ MPa, and their errors given by the 95% confidence bound of the adjusted parameters. From σ_0 we obtain the shear friction $\tau_0 = 0.52 \pm 0.04$ MPa, which compares well with the Peierls barrier for aluminum (Kamimura et al., 2013).

The result of this analysis is summarized in Fig. 8, where we present σ versus the Taylor stress $\sigma_{Taylor} = \sigma_0 + \alpha M b G \sqrt{\Lambda}$. The raw data is presented for the three consecutive tensile tests with $\sigma > \sigma_Y$. We also present a set of average values calculated by segmenting the data into 20 equally spaced bins. The data collapses well onto the straight line $\sigma = \sigma_{Taylor}$, showing that indeed workhardening occurs in our sample. We stress that $\alpha \approx 0.17$ and $\tau_0 \approx 0.52$ MPa fit well with the expected values,
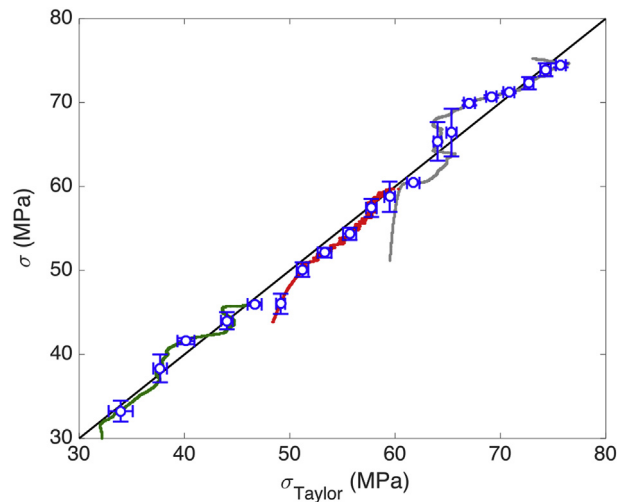
Fig. 8. Applied stress σ versus Taylor stress $\sigma_{\text{Taylor}} = \sigma_0 + \alpha MbG\sqrt{\Lambda}$. The continuous color lines correspond to data of the three consecutive tensile tests with $\sigma > \sigma_Y$ (test 1, green; test 2, red; test 3, gray). The continuous black straight line shows the relation $\sigma = \sigma_{\text{Taylor}}$. The symbols are averages over windows for both quantities, obtained from 20 bins defined from the minimum and maximum measured Λ. Error bars correspond to standard deviations. (For interpretation of the references to colour in this figure legend, the reader is referred to the web version of this article.)

which makes a strong case for our procedure to determine a continuous relation between the absolute value of dislocation density, Λ, and the applied stress, σ.

To conclude, we stress that the fact that our data follows the Taylor rule is quite robust with respect to the precise value of L that is used to obtain Λ. If we scale $L \rightarrow \delta L$, then it is straight forward to show that the data still obeys the Taylor rule with the same adjusted σ_0 but with a new constant $\alpha \rightarrow \alpha/\delta$. Thus, considering the minimum and maximum average L presented in Table 2, such that $\delta \approx 0.61$ and $\delta = 1.8$, respectively, we conclude that α can take values between ≈ 0.28 and ≈ 0.1 respectively, which are quite reasonable. In fact, theorical calculations give α values between 0.05 and 1.3 and experimental results are between 0.2 and 1.1 (Viguier, 2003). The value $\alpha = 0.28$ is associated with the interaction between an edge dislocation and a dislocation forest, while $\alpha = 0.1$ is associated with a similar interaction involving mixed type dislocations (Lavrentev, 1980).

5. Conclusion

In this work we have reported measurements of the speed of transverse waves as a function of applied stress obtained in real time for an aluminum sample undergoing a standard tension test. Using Eqn. (5) we can infer a value for the dimensionless quantity ΛL^2, the product of the dislocation density Λ (in units of inverse surface area) and the square of the (average) dislocations segment length L. This quantity appears because the model that is used to obtain the formula is based on dislocation segments of length L oscillating in response to the loading provided by an elastic wave.

The onset of plasticity in aluminum, as determined by the yield stress, is accompanied by a marked decrease in the speed of transverse waves. This is not only consistent with a proliferation of dislocations, but also provides a continuous and quantitative relationship between the dislocation density and externally applied stress. The traditional methods to measure dislocation density at the macroscale, such as XRD or TEM, are not able to provide such a continuous link because their intrusive nature only allows for before-and-after measurements. They do, however, provide an independent yardstick to validate the acoustics measurements. Significantly, there is very good agreement between the reported measurements and the Taylor rule. We believe this agreement provides strong support and validation for the proposed methodology.

The motivation leading to the present work was to develop a non-destructive ultrasonic tool to characterize ductile failure as is done with brittle fracture. In the case of brittle fracture, a major use of ultrasound as a non-destructive testing tool lies not so much in the characterization of catastrophic crack propagation at the failure point itself, but in the early detection, at stresses lower than the fracture strength, of microcraks and flaws that signal the danger that failure may occur. The success of this technique lies in the accurate characterization of the interaction of elastic waves with cracks and flaws. We have reported results that show how to use ultrasound as a non-destructive testing tool to characterize the onset and subsequent evolution of plastic behavior in metals and not so much, at least for now, to characterize the failure point itself, which is preceded by the formation of dislocation pile-ups and microvoids. This characterization of the onset of plastic behavior has been achieved through non-invasive and continuous measurement of the dislocation density as a function of stress. We are aware of no other experimental results that can provide similar information. Finally, the interaction of voids with acoustic waves is well known, so an interesting future development could be to include this void-sound interaction to the analysis of acoustic signals to characterize the appearance of voids.

Acknowledgments

Appendix. 6.

6.1. The Rietveld method

Since the 60's, the Rietveld method has been extensively developed and used to find structural and microstructural parameters for polycrystalline materials. X-ray diffraction peak profile analysis has become a powerful tool. This method has been successfully applied to a wide variety of materials (metals, alloys, ceramics and polymers), and is based on the minimization of a residual function using a non-linear least squares algorithm considering physical parameters involved in the XRD phenomenon. More specifically, the method fits the structural and microstructural parameters minimizing the error function

$$S_y = \sum_{i=1}^{N} w_i |Y_0(2\theta_i) - Y_c(2\theta_i)|^2, \tag{9}$$

where $Y_0(2\theta_i)$ and $Y_c(2\theta_i)$ are observed and calculated intensities, respectively, and $w_i = 1/Y_0(2\theta_i)$. The profile of a X-ray powder pattern $Y_c(2\theta_i)$ can be well described by a convolution

$$Y_c(2\theta_i) = Y_{bi}(2\theta_i) + S_F \sum_{j=1}^{N_{ph}} \frac{f_j}{V_j^2} \sum_{k=1}^{N_{uc}} \left[Lp_k \left| F_{j,k} \right|^2 CS_j \left(2\theta_i - 2\theta_{k,j} \right) A_j P_{k,j} \right], \tag{10}$$

where the j indices refer to the different phases that can be present and the indices k to the unit cells. Y_{bi} is a polynomial function of background, S_F is the beam intensity, f_j is the volume fraction of each phase, V_j is the volume of unit cell of each phase, Lp is the Lorentz-polarization factor, $F_{j,k}$ is the structure factor, CS_j is related with crystallite size and microstrains, A_j is the X-ray material absorption and $P_{j,k}$ quantifies the texture. An X-ray pattern depends on phases (crystal structure, microstructure, quantity, cell volume, texture, stress, chemistry), instrument geometry characteristics (beam intensity, Lorentz-Polarization, background, resolution, aberrations, radiation) and sample (position, shape and dimension, orientation). So each variable can be refined to obtain the optimized value. The first term on the right of Eqn. (10) gives the influence of the background and the remaining terms are given by the intensities of reflections in the XRD pattern.

6.1.1. Background $Y_{bi}(2\theta)$
Generally, a polynomial function in 2θ is used to determine the background,

$$Y_{bi}(2\theta) = \sum_{n=0}^{N_b} a_n (2\theta)^n, \tag{11}$$

where N_b is the polynomial degree and a_n are the polynomial coefficients.

6.1.2. Scale factor S_j
This factor must be determined for each phase present in XRD pattern. The scale factor influence is defined as

$$S_j = S_F \frac{f_j}{V_j^2}, \tag{12}$$

where S_F is the beam intensity and depends on the measurement, f_j is the phase volume fraction and V_j is the phase cell volume.

6.1.3. Lorentz-Polarization factor Lp_k
The XRD measurements are influenced by instrument, geometry, monochromator, detector, beam size to sample volume and sample position. Thus, the intensity of reflections is a function of 2θ. For the Bragg-Brentano configuration this factor is expressed as

$$Lp_k = \frac{1 + \cos^2(2\theta)}{\sin^2(\theta)\cos(\theta)}. \tag{13}$$

6.1.4. Structure factor $F_{k,j}$

The structure factor takes into account the resultant wave scattered by all atoms of the unit cell. It is the summation of all waves scattered by individual atoms in the unit cell and depends on crystal structure, multiplicity factor m_k and temperature factor B_n. The expression of the structure factor is given by

$$\left|F_{k,j}\right|^2 = m_k \left| \sum_{n=1}^{N_a} f_n e^{-B_n \frac{\sin^2(\theta)}{\lambda_{XRD}}} e^{2\pi i(hx_n+ky_n+lz_n)} \right|^2, \tag{14}$$

where m_k is the multiplicity of the k reflection with (hkl) Miller indices, N_a is the number of atoms in unit cell, x_n, y_n, z_n are the coordinates of the $n-$ th atom, λ_{XRD} is the X-ray wavelength and f_n is the atomic scattering factor.

6.1.5. Absorption factor A_j

The intensities of reflections are affected by the sample's absorption. In the Bragg-Brentano configuration the absorption factor is

$$A_j = \frac{1}{2\mu_a}, \tag{15}$$

where μ_a is the linear absorption coefficient of the sample.

6.1.6. Texture $P_{k,j}$

Texture in polycrystalline samples refers to the distinct spatial orientation of the individual crystallites within the material. This contribution is taken into account by the $P_{k,j}$ factor. There are several models that can be applied to obtain the texture effect: arbitrary, harmonic, March-Dollase, E-WIMV, standard function, WIM, etc. We have used the arbitrary texture model.

6.1.7. Profile shape function $(2\theta_i - 2\theta_{k,j})$

The profile shape is a function of the sample (crystallite size, microstrain, crystalline defect) and the instrument (radiation source, geometry, slit sizes), and varies with the elevation angle 2θ. The typical profile shape functions that are used are Gauss, Lorentz, Pseudo-Voigt and Person VII. We use the Pseudo-Voigt function, which is widely used for metals because it gives a better fit of the peak tails,

$$PV\left(2\theta_i - 2\theta_{k,j}\right) = I_n \left[\left(\frac{\eta_k}{1 + S_{i,\{k,j\}}^2} + (1 - \eta_k)e^{-S_{i,\{k,j\}}^2 \ln 2} \right) \right], \tag{16}$$

where I_n is the intensity, $S_{i,\{k,j\}}$ is defined as $(2\theta_i - 2\theta_{k,j})/\omega_{k,j}$, $\omega_{k,j}$ is the Caglioti formula given as $\omega_{k,j} = W + V\tan\theta_{k,j} + U\tan2\theta_{k,j}$ (W, V, U are experimental parameters) and η_k is the gaussianity factor determined as $\eta_k = \sum_{n=1}^{n_p} c_n (2\theta)^n$ (c_n and n_p are experimental parameters).

6.1.8. Crystallite size and microstrain effects CS_j

The broadening of reflections occurs due to the convoluted effects of crystallite size and microstrain. The microstrain is produced by crystalline defects, mainly dislocations. In the case of isotropic broadening, the microstrain (ε) and crystallite size (D) can be determined using the Delft model (which gives the integral breadths for the Gaussian and Lorentzian components in the reflections). For anisotropic broadening of reflections, the dependence of microstrain and crystallite size on miller indices are given by the Popa rules (Popa, 1998).

6.1.9. Refinement quality (R-values)

It is important to know the evolution and the quality of the refinement. The best way of following a refinement is to observe the difference profile plot (McCusker et al., 1999). There are indicators that determine the quality of the refinement, called R-values. Two such values are defined: the weighted-profile value

$$R_{wp} = \left(\frac{\sum_{i=1}^N w_i [Y_0(2\theta_i) - Y_c(2\theta_i)]^2}{\sum_{i=1}^N w_i Y_0(2\theta_i)^2} \right)^{1/2}. \tag{17}$$

and

$$R_{exp} = \left(\frac{N - P}{\sum_{i=1}^N w_i Y_0(2\theta_i)^2} \right)^{1/2}, \tag{18}$$

where N is the number of observations and P the number of parameters. The R_{exp} value accounts for the quality of the data (i.e. the counting statistics).

The R_{wp} value is statistically the most meaningful indicator of the overall fit since the numerator is the residual that is minimized in the least squares procedure. Another important parameter is the goodness of fit, $\chi^2 = R_{wp}/R_{exp}$. A refinement is considered excellent when $1 < \chi^2 < 2$. The χ^2 values obtained for the refinements of *Ori*, *PB* and *PW* samples are 1.29, 0.99 and 1.7, respectively, which show that our refinements are of high quality. On the other hand, the estimated errors of $\langle \varepsilon^2 \rangle^{1/2}$ are between one to three orders of magnitude smaller than their averages, as shown in Table 1. Considering the good χ^2 values and the small errors of $\langle \varepsilon^2 \rangle^{1/2}$, it is expected to obtain acceptable dislocation density values within an order of magnitude. Therefore, the propagated error using Eqn. (2) is small.

References

Abbaschian, R., Reed-Hill, R., 2008. Physical Metallurgy Principles. Cengage Learning.

Adler, R.P.I., Otte, H.M., 1966. Dislocation configurations in wire-drawn polycrystalline copper alloys: a study by x-ray diffraction. Mater. Sci. Eng. 1 (4), 222–238. http://dx.doi.org/10.1016/0025-5416(66)90034-6.

Adler, R.P.I., Otte, H.M., Wagner, C.N.J., 1970. Determination of dislocation density and stacking fault probability from x-ray powder pattern peak profiles. Metall. Trans. 1 (9), 2375–2382. http://dx.doi.org/10.1007/BF03038366.

Arsenlis, A., Parks, D.M., Becker, R., Bulatov, V.V., 2004. On the evolution of crystallographic dislocation density in non-homogeneously deforming crystals. J. Mech. Phys. Solids 52 (6), 1213–1246. http://dx.doi.org/10.1016/j.jmps.2003.12.007.

ASTM, 2013. Standard Test Methods for Tension Testing of Metallic Materials. ASTM E8/E8M-13a. ASTM International, West Conshohocken, PA.

Barra, F., Espinoza-González, R., Fernández, H., Lund, F., Maurel, A., Pagneux, V., 2015. The use of ultrasound to measure dislocation density. JOM 67 (8), 1856–1863. http://dx.doi.org/10.1007/s11837-015-1458-9.

Bulatov, V.V., Hsiung, L.L., Tang, M., Arsenlis, A., Bartelt, M.C., Cai, W., Florando, J.N., Hiratani, M., Rhee, M., Hommes, G., Pierce, T.G., de la Rubia, T.D., 2006. Dislocation multi-junctions and strain hardening. Nature 440, 1174–1178. http://dx.doi.org/10.1038/nature04658.

Chen, C.-H., 2007. Ultrasonic and Advanced Methods for Nondestructive Testing and Material Characterization. World Scientific, Singapore, Reading, Massachusetts. http://dx.doi.org/10.1142/6327.

Christensen, R.M., 2008. Observations on the definition of yield stress. Acta Mech. 196 (3), 239–244. http://dx.doi.org/10.1007/s00707-007-0478-0.

Devincre, B., Hoc, T., Kubin, L., 2008. Dislocation mean free paths and strain hardening of crystals, 320 (5884), 1745–1748. http://dx.doi.org/10.1126/science.1156101.

Granato, A., Lücke, K., 1956. Theory of mechanical damping due to dislocations. J. Appl. Phys. 27 (6), 583–593. http://dx.doi.org/10.1063/1.1722436.

Granato, A., Lücke, K., 1956. Application of dislocation theory to internal friction phenomena at high frequencies. J. Appl. Phys. 27 (7), 789–805. http://dx.doi.org/10.1063/1.1722485.

Gubicza, J., Chinh, N., Csanádi, T., Langdon, T., Ungár, T., 2007. Microstructure and strength of severely deformed fcc metals. Mater. Sci. Eng. A 462 (12), 86–90 international Symposium on Physics of Materials, 2005. http://doi.org/10.1016/j.msea.2006.02.455.

Guery, A., Hild, F., Latourte, F., Roux, S., 2016. Slip activities in polycrystals determined by coupling DIC measurements with crystal plasticity calculations. Int. J. Plasticity 81, 249–266. http://dx.doi.org/10.1016/j.ijplas.2016.01.008.

Hirth, J.P., 2012. Dislocations and pinning points. J. Supercond. Nov. Magnetism 25 (3), 561–563. http://dx.doi.org/10.1007/s10948-012-1481-9.

Hirao, M., Ogi, H., Suzuki, N., Ohtani, T., 2000. Ultrasonic attenuation peak during fatigue of polycrystalline copper. Acta Mater. 48 (2), 517–524. http://dx.doi.org/10.1016/S1359–6454(99)00346–8.

Kahloun, C., Le, L., Monnet, G., Chavanne, M.H., Ait, E., Franciosi, P., 2013. Topological analysis of 110 slip in an iron crystal from in situ atomic force microscopy. Acta Mater. 61 (17), 6453–6465. http://dx.doi.org/10.1016/j.actamat.2013.07.023.

Kahloun, C., Monnet, G., Queyreau, S., Le, L., Franciosi, P., 2016. A comparison of collective dislocation motion from single slip quantitative topographic analysis during in-situ AFM room temperature tensile tests on Cu and Fe crystals. Int. J. Plasticity 84, 277–298. http://dx.doi.org/10.1016/j.ijplas.2016.06.002.

Kamimura, Y., Edagawa, K., Takeuchi, S., 2013. Experimental evaluation of the Peierls stresses in a variety of crystals and their relation to the crystal structure. Acta Mater. 61 (1), 294–309. http://dx.doi.org/10.1016/j.actamat.2012.09.059.

Krivoglaz, M.A., 1969. Theory of X-ray and Thermal Neutron Scattering by Real Crystals. Plenum Press, New York.

Kubin, L., Devincre, B., Hoc, T., 2008. Toward a physical model for strain hardening in fcc crystals. Mater. Sci. Eng. A 483 484, 19–24, 14th International Conference on the Strength of Materials. http://doi.org/10.1016/j.msea.2007.01.167.

Kuhlmann-Wilsdorf, D., 1985. Theory of workhardening 1934-1984. Metall. Trans. A 16 (12), 2091–2108. http://dx.doi.org/10.1007/BF02670414.

Landau, P., Shneck, R.Z., Makov, G., Venkert, A., 2010. In-situ tem study of dislocation patterning during deformation in single crystal aluminum. J. Phys. Conf. Ser. 241 (1), 012060. http://dx.doi.org/10.1088/1742-6596/241/1/012060.

Lavrentev, F., 1980. The type of dislocation interaction as the factor determining work hardening. Mater. Sci. Eng. 46 (2), 191–208. http://dx.doi.org/10.1016/0025-5416(80)90175-5.

Ledbetter, H., Fortunko, C., Heyliger, P., 2011. Elastic constants and internal friction of polycrystalline copper. J. Mater. Res. 10 (6), 1352–1353. http://dx.doi.org/10.1557/JMR.1995.1352.

Lee, M., Lim, H., Adams, B., Hirth, J., Wagoner, R., 2010. A dislocation density-based single crystal constitutive equation. Int. J. Plasticity 26 (7), 925–938. http://dx.doi.org/10.1016/j.ijplas.2009.11.004.

Leisure, R.G., Willis, F.A., 1997. Resonant ultrasound spectroscopy. J. Phys. Condens. Matter 9 (28), 6001. http://dx.doi.org/10.1088/0953-8984/9/28/002.

Leung, H., Ngan, A., 2016. Dislocation-density function dynamics an all-dislocation, full-dynamics approach for modeling intensive dislocation structures. J. Mech. Phys. Solids 91, 172–203. http://dx.doi.org/10.1016/j.jmps.2016.03.008.

Leung, H., Leung, P., Cheng, B., Ngan, A., 2015. A new dislocation-density-function dynamics scheme for computational crystal plasticity by explicit consideration of dislocation elastic interactions. Int. J. Plasticity 67, 1–25. http://dx.doi.org/10.1016/j.ijplas.2014.09.009.

Lutterotti, L., Scardi, P., 1990. Simultaneous structure and size–strain refinement by the Rietveld method. J. Appl. Crystallogr. 23 (4), 246–252. http://dx.doi.org/10.1107/S0021889890002382.

Maurel, A., Mercier, J.-F., Lund, F., 2004. Scattering of an elastic wave by a single dislocation. J. Acoust. Soc. Am. 115 (6), 2773–2780. http://dx.doi.org/10.1121/1.1687735.

Maurel, A., Pagneux, V., Barra, F., Lund, F., 2005. Wave propagation through a random array of pinned dislocations: velocity change and attenuation in a generalized Granato and Lücke theory. Phys. Rev. B 72, 174111. http://dx.doi.org/10.1103/PhysRevB.72.174111.

McCusker, L.B., Von Dreele, R.B., Cox, D.E., Louër, D., Scardi, P., 1999. Rietveld refinement guidelines. J. Appl. Crystallogr. 32 (1), 36–50. http://dx.doi.org/10.1107/S0021889898009856.

McSkimin, H.J., 1961. Pulse superposition method for measuring ultrasonic wave velocities in solids. J. Acoust. Soc. Am. 33 (1), 12–16. http://dx.doi.org/10.1121/1.1908386.

Migliori, A., Sarrao, J., Visscher, W.M., Bell, T., Lei, M., Fisk, Z., Leisure, R., 1993. Resonant ultrasound spectroscopic techniques for measurement of the elastic moduli of solids. Physica B Condens. Matter 183 (1), 1–24. http://dx.doi.org/10.1016/0921-4526(93)90048-B.

Min, X., Kato, H., 2004. Change in ultrasonic parameters with loading/unloading process in cyclic loading of aluminium alloy. Mater. Sci. Eng. A 372 (1–2), 269–277. http://dx.doi.org/10.1016/j.msea.2004.01.033.

Min, X.-H., Kato, H., Narisawa, N., Kageyama, K., 2005. Real-time ultrasonic measurement during tensile testing of aluminum alloys. Mater. Sci. Eng. A 392 (1–2), 87–93. http://dx.doi.org/10.1016/j.msea.2004.10.019.

Mittemeijer, E.J., Scardi, P., 2004. Diffraction Analysis of the Microstructure of Materials. Springer-Verlag, Berlin Heidelberg.

Monavari, M., Sandfeld, S., Zaiser, M., 2016. Continuum representation of systems of dislocation lines: a general method for deriving closed-form evolution equations. J. Mech. Phys. Solids 95, 575–601. http://dx.doi.org/10.1016/j.jmps.2016.05.009.

Mujica, N., Cerda, M.T., Espinoza, R., Lisoni, J., Lund, F., 2012. Ultrasound as a probe of dislocation density in aluminum. Acta Mater. 60 (16), 5828–5837. http://dx.doi.org/10.1016/j.actamat.2012.07.023.

Ogi, H., Ledbetter, H., Kim, S., Hirao, M., 1999. Contactless mode-selective resonance ultrasound spectroscopy: electromagnetic acoustic resonance. J. Acoust. Soc. Am. 106 (2), 660–665. http://dx.doi.org/10.1121/1.427607.

Ogi, H., Sato, K., Asada, T., Hirao, M., 2002. Complete mode identification for resonance ultrasound spectroscopy. J. Acoust. Soc. Am. 112 (6), 2553–2557. http://dx.doi.org/10.1121/1.1512700.

Ogi, H., Nakamura, N., Hirao, M., Ledbetter, H., 2004. Determination of elastic, anelastic, and piezoelectric coefficients of piezoelectric materials from a single specimen by acoustic resonance spectroscopy. Ultrasonics 42 (1–9), 183–187. Proceedings of Ultrasonics International 2003. http://dx.doi.org/10.1016/j.ultras.2004.01.007.

Oh, S.H., Legros, M., Kiener, D., Dehm, G., 2009. In situ observation of dislocation nucleation and escape in a submicrometre aluminium single crystal. Nat. Mater. 8 (2), 95–100. http://dx.doi.org/10.1038/nmat2370.

Popa, N.C., 1998. The (hkl) dependence of diffraction-line broadening caused by strain and size for all Laue groups in Rietveld refinement. J. Appl. Crystallogr. 31 (2), 176–180. http://dx.doi.org/10.1107/S0021889897009795.

Rodríguez, N., Maurel, A., Pagneux, V., Barra, F., Lund, F., 2009. Interaction between elastic waves and prismatic dislocation loops. J. Appl. Phys. 106 (5), 054910–054919. http://dx.doi.org/10.1063/1.3213338.

Rudolf, C., Boesl, B., Agarwal, A., 2016. In situ mechanical testing techniques for real-time materials deformation characterization. JOM 68 (1), 136–142. http://dx.doi.org/10.1007/s11837-015-1629-8.

Scardi, P., Lutterotti, L., Maistrelli, P., 1994. Experimental determination of the instrumental broadening in the Bragg Brentano geometry. Powder Diffr. 9, 180–186. http://dx.doi.org/10.1017/S0885715600019187.

Seeger, A., Kronmuller, H., 1962. Stored energy and recovery of deformed F.C.C. metals. Philos. Mag. 7 (78), 897–913. http://dx.doi.org/10.1080/14786436208212888.

Sills, R.B., Aghaei, A., Cai, W., 2016. Advanced time integration algorithms for dislocation dynamics simulations of work hardening. Model. Simul. Mater. Sci. Eng. 24, 1–17. http://dx.doi.org/10.1088/0965-0393/24/4/045019.

Sobie, C., Capolungo, L., McDowell, D.L., Martinez, E., 2017. Modal analysis of dislocation vibration and reaction attempt frequency. Acta Mater. http://doi.org/10.1016/j.actamat.2017.02.005.

Ungár, T., Gubicza, J., Ribárik, G., Borbély, A., 2001. Crystallite size distribution and dislocation structure determined by diffraction profile analysis: principles and practical application to cubic and hexagonal crystals. J. Appl. Crystallogr. 34 (3), 298–310. http://dx.doi.org/10.1107/S0021889801003715.

Viguier, B., 2003. Dislocation densities and strain hardening rate in some intermetallic compounds. Mater. Sci. Eng. A 349 (12), 132–135. http://doi.org/10.1016/S0921-5093(02)00785-2.

Wang, S.C., Zhu, Z., Starink, M.J., 2004. Estimation of dislocation densities in cold rolled Al-Mg-Cu-Mn alloys by combination of yield strength data, EBSD and strength models. J. Microsc. 217, 174–178. http://dx.doi.org/10.1111/j.1365-2818.2005.01449.x.

Will, G., 2006. Powder Diffraction: the Rietveld Method and the Two-stage Method. Springer-Verlag, Berlin Heidelberg.

Williams, D.B., Carter, C.B., 2009. Transmission Electron Microscopy. Springer, US.

Williamson, G.K., Smallman III, R.E., 1956. Dislocation densities in some annealed and cold-worked metals from measurements on the x-ray debye-scherrer spectrum. Philos. Mag. 1 (1), 34–46. http://dx.doi.org/10.1080/14786435608238074.

Zaiser, M., Sandfeld, S., 2014. Scaling properties of dislocation simulations in the similitude regime. Model. Simul. Mater. Sci. Eng. 22 (6), 065012.

Zhang, X.-G., Simpson, W.A., Vitek, J.M., Barnard, D.J., Tweed, L.J., Foley, J., 2004. Ultrasonic attenuation due to grain boundary scattering in copper and copper-aluminum. J. Acoust. Soc. Am. 116 (1), 109–116. http://dx.doi.org/10.1121/1.1744752.

Zhang, L., Sekido, N., Ohmura, T., 2014. Real time correlation between flow stress and dislocation density in steel during deformation. Mater. Sci. Eng. A 611, 188–193. http://dx.doi.org/10.1016/j.msea.2014.05.073.